A High-Sensitivity AlGaN/GaN HEMT Terahertz Detector With Integrated Broadband Bow-Tie Antenna

Maris Bauer [iD], Adam Rämer [iD], Serguei A. Chevtchenko, Konstantin Y. Osipov, Dovilė Čibiraitė [iD], Sandra Pralgauskaitė [iD], Kęstutis Ikamas [iD], Alvydas Lisauskas [iD], *Member, IEEE*, Wolfgang Heinrich [iD], *Fellow, IEEE*, Viktor Krozer [iD], *Senior Member, IEEE*, and Hartmut G. Roskos [iD]

(Invited Paper)

Abstract—**Many emerging applications in the terahertz (THz) frequency range demand highly sensitive, broadband detectors for room-temperature operation. Field-effect transistors with integrated antennas for THz detection (TeraFETs) have proven to meet these requirements, at the same time offering great potential for scalability, high-speed operation, and functional integrability.**

M. Bauer was with Physikalisches Institut, Johann Wolfgang Goethe-Universität, D-60438 Frankfurt am Main, Germany. He is now with the Center for Materials Characterization and Testing, Fraunhofer ITWM, D-67663 Kaiserslautern, Germany (e-mail: maris.bauer@itwm.fraunhofer.de).

A. Rämer, S. A. Chevtchenko, K. Y. Osipov, and W. Heinrich are with Ferdinand-Braun-Institut, Leibniz-Institut für Höchstfrequenztechnik (FBH), D-12489 Berlin, Germany (e-mail: adam.raemer@fbh-berlin.de; sergey.shevchenko@fbh-berlin.de; konstantin.osipov@ampleon.com; wolfgang.heinrich@fbh-berlin.de).

D. Čibiraitė and H. G. Roskos are with Physikalisches Institut, Johann Wolfgang Goethe-Universität, D-60438 Frankfurt am Main, Germany (e-mail: cibiraite@physik.uni-frankfurt.de; roskos@physik.uni-frankfurt.de).

S. Pralgauskaitė is with Institute of Applied Electrodynamics and Telecommunications, Vilnius University, LT-10257 Vilnius, Lithuania (e-mail: sandra.pralgauskaite@ff.vu.lt).

K. Ikamas is with Institute of Applied Electrodynamics and Telecommunications, Vilnius University, LT-10257 Vilnius, Lithuania, and also with the General Jonas Žemaitis Military Academy of Lithuania, LT-10322 Vilnius, Lithuania (e-mail: kestutis.ikamas@ff.vu.lt).

A. Lisauskas was with Physikalisches Institut, Johann Wolfgang Goethe-Universität, D-60438 Frankfurt am Main, Germany. He is now with the Institute of Applied Electrodynamics and Telecommunications, Vilnius University, LT-10257 Vilnius, Lithuania, and also with the Center for Terahertz Research and Applications, Institute of High Pressure Physics PAS, PL-01-142 Warsaw, Poland (e-mail: alvydas.lisauskas@ff.vu.lt).

V. Krozer is with Physikalisches Institut, Johann Wolfgang Goethe-Universität, D-60438 Frankfurt am Main, Germany, and also with Ferdinand-Braun-Institut, Leibniz-Institut für Höchstfrequenztechnik (FBH), D-12489 Berlin, Germany (e-mail: krozer@physik.uni-frankfurt.de).

Color versions of one or more of the figures in this paper are available online at http://ieeexplore.ieee.org.

Digital Object Identifier 10.1109/TTHZ.2019.2917782

In this contribution, we report on an optimized field-effect transistor with integrated broadband bow-tie antenna for THz detection (bow-tie TeraFET) and compare the detector's performance to other state-of-the-art broadband THz detector technologies. Implemented in a recently developed AlGaN/GaN MMIC process, the presented TeraFET shows a more than twice performance improvement compared to previously fabricated AlGaN/GaN-HEMT-based TeraFETs. The detector design is the result of detailed modeling of the plasma-wave-based detection principle embedded in a full-device detector model to account for power coupling of the THz radiation to the intrinsic gated FET channel. The model considers parasitic circuit elements as well as the high-frequency impedance of the integrated broadband antenna, and also includes optical losses from a silicon substrate lens. Calibrated characterization measurements have been performed at room temperature between 490 and 645 GHz, where we find values of the *optical* (total beam power referenced) noise-equivalent power of 25 and 31 pW$/\sqrt{\text{Hz}}$ at 504 and 600 GHz, respectively, in good agreement with simulation results. We then show the broadband detection capability of our AlGaN/GaN detectors in the range from 0.2 to 1.2 THz and compare the TeraFETs' signal-to-noise ratio to that of a Golay cell and a photomixer. Finally, we demonstrate an imaging application in reflection geometry at 504 GHz and determine a dynamic range of >40 dB.

Index Terms—**Broadband antenna, field-effect transistors, GaN HEMT, plasmonic mixing, terahertz (THz) detectors.**

I. Introduction

THE development of detectors for the terahertz (THz) frequency range is a dynamic field of research with a strong focus on such approaches that combine high sensitivity, high speed, cost effectiveness, and ease of use. In particular, room-temperature operation is desired. Besides other semiconductor-based detector technologies (e.g., uncooled microbolometers [1]–[5], Schottky-diode-based rectifiers (SBD) [6]–[8], Sb-heterojunction backward diodes [9]–[11], resonant-tunneling diodes [12], [13], broken-symmetry nano-channel detectors [14], or thermoelectric detectors [15]), THz detection with antenna-coupled field-effect transistors (TeraFETs) has emerged as a powerful concept, which meets the aforementioned requirements [16]–[22]. The underlying detection principle is rectification by resistive self-mixing in the two-dimensional electron gas (2DEG) in the transistor's channel, modified by

the occurrence of charge density (plasma) waves at frequencies in the THz range [23], [24]. The existence of plasma effects was first suggested in the early 1990s by Dyakonov and Shur [25], who predicted a rectifying action of the plasma waves leading to a THz-induced dc photocurrent (or voltage) along the channel. Plasmonic effects are a subject of active research in the field of submillimeter-wave and THz electronic devices, since they promise device operation beyond conventional frequency limits, such as the classical transit frequency $f_{\max}$ of field-effect transistors (FETs) [24]–[26]. They can be exploited for the realization of *direct* detectors whose dc voltage or current response is proportional to the beam power, for heterodyne detection [27]–[30], and even as nonlinear elements for correlation measurements of THz pulses [31]. The theoretical description of the plasma wave modified rectification in the FET's channel is based on a hydrodynamic transport model [25], which has led to the term *plasma wave detectors* in subsequent research.

TeraFET detectors have been realized in various material systems and with different integrated antenna designs both for narrow-band and broadband operation, e.g., [22] and [32]–[41]. The most sensitive TeraFETs have been fabricated in silicon CMOS—mainly due to the maturity of the fabrication technology—for which state-of-the-art device sensitivities expressed in values of the optical noise-equivalent power (NEP) (i.e., not corrected for the detector area, see in the following) of around 10 pW/$\sqrt{\text{Hz}}$ for narrow-band detectors [32], [33] and of about 50 pW/$\sqrt{\text{Hz}}$ for wideband detectors [36] have been reported. In spite of its many advantages—not least the potential for a high degree of functional integration [21], [42]—Si-CMOS has some technological downsides, for instance, a high electrostatic discharge sensitivity due to a limited breakdown voltage. A recently published review article provides an overview of silicon-based THz technologies [22].

As an alternative, GaN technology has emerged as a promising candidate to overcome some of the technological and application-related challenges. AlGaN/GaN high-electron-mobility transistors (HEMTs) provide a number of beneficial physical properties, such as a high 2DEG sheet carrier density and an enhanced saturation velocity in combination with high robustness in breakdown voltage and radiation hardness to ionizing radiation—of interest in particular with respect to space applications [43]. The properties of AlGaN/GaN HEMTs can facilitate impedance matching in the integration of broadband antenna designs due to relatively low intrinsic channel impedances. Successful implementations of TeraFETs based on AlGaN/GaN HEMTs have previously been demonstrated in a number of papers [31], [35], [38], [44]–[55] exhibiting, for the best detectors, sensitivity values roughly a factor of four to five worse than those of the best narrow-band Si-based TeraFETs.

In this paper, we present optimized broadband TeraFET detectors implemented in a recently developed GaN MMIC process, which exhibit an improved sensitivity almost comparable to that of state-of-the-art Si-CMOS TeraFETs. In Section II, we first present a device model, which considers power coupling under realistic device (impedance) conditions. We present results of simulations for the anticipated THz detection performance of TeraFETs influenced by a number of high-frequency factors

specific to the detector circuit. We then discuss the design and fabrication of TeraFETs with integrated bow-tie antennas in Section III, and present in Section IV the extraction of fundamental device parameters from measured dc resistance data, based on a semiempirical charge control model. Sections V and VI address the experimental characterization of the fabricated AlGaN/GaN TeraFETs over a broad frequency range from 0.4 to 1.2 THz. The obtained experimental findings are compared to the simulated THz responsivity and NEP values, where we also show that our AlGaN/GaN TeraFETs achieve a very competitive state-of-the-art performance. They provide higher sensitivity than commercially available pyroelectric and acousto-optic detectors working at room temperature, and that they compare well with the best broadband Schottky diode detectors [7], [8]. Finally, in Section VII, we demonstrate application of the high-sensitivity detectors in a reflection imaging setup using a Schwarzschild telescope objective.

II. DEVICE MODELING

In this section, we describe the TeraFET device model used for the calculation of the anticipated THz response and TeraFET sensitivity. For low frequencies—below approximately 100 GHz—the detector can be described by quasi-static analysis and treated as a lumped element model. One example for such a treatment is the Volterra-series-based modeling as described, e.g., in [56]. However, toward higher frequencies, such models have to be extended by additional device elements toward distributed element circuits. A different approach, is the treatment of the intrinsic TeraFET detection mechanism by a physics-based charge carrier transport model. In 1996, Dyakonov and Shur [25] proposed the use of a reduced[1] hydrodynamic transport model to describe the dynamics of the 2DEG in the channel of an FET under the influence of a THz signal, and discussed the possibility of plasma-wave-based resonant and nonresonant detection of THz radiation by nonlinear self-mixing of the THz wave involving plasma waves induced in the 2DEG under the gate. Due to the nature of this process, it is often referred to as *plasma-wave-based* or *plasmonic* THz detection. The term *TeraFET* is used to distinguish the detector device as a whole—commonly including an integrated antenna structure for efficient coupling of the THz radiation—from the intrinsic FET alone.

For plasma-wave-based THz detection, the term *nonresonant* detection was introduced for the case of overdamped plasma waves in the gated channel or for the case where the gated channel is too long, so that the waves can propagate only over a fraction of its length before decaying. In this situation, standing waves cannot build up and the device's intrinsic photoresponse is broadband. THz detection with TeraFETs has been demonstrated for frequencies as high as 22 THz [61].

In contrast, if the lifetime of the plasma wave is long enough for the formation of a standing-wave pattern due to wave reflection at the ends of the gated channel, the detection regime

---

[1]The simplification of the model lies in the omission of diffusive terms in the transport model. Recent experiments show that a significant contribution of diffusive currents to the detection signal can be present [41], [57]–[60], also see text footnote 6.
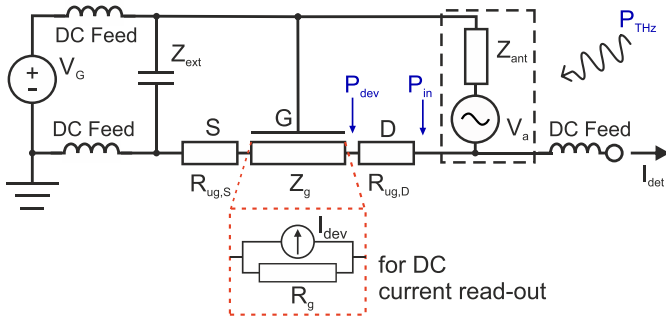
Fig. 1.   Equivalent circuit of AlGaN/GaN TeraFETs for gate-drain coupling. Incorporation of an external gate-source shunting capacitance Z_{ext} pins the gate and the source side of the gated channel to ac ground. For the description of the read-out of the rectified signal, the gated channel region is replaced by an ideal current source with an internal resistance R_{g} (as shown in the box plotted with a red dashed line).

is termed *resonant*. The interference can be of constructive or destructive nature. For frequencies with constructive wave interference, Dyakonov and Shur predicted significant enhancement of plasmonic rectification [25], expressed in high values of the so-called plasmonic efficiency factor $f(\omega)$ at the resonance frequencies [25], [34]. This prediction stimulated the search for ultra-sensitive TeraFETs fabricated on the basis of materials with high carrier mobility [62]–[67]. On the other hand, up to now, little experimental evidence exists that a significant enhancement can be expected for real TeraFET devices. One reason may be the (in-)efficiency of power coupling to the active device element, i.e., the FET's gated channel region. At frequencies of plasma wave resonances, this coupling in real devices depends not only on $f(\omega)$ alone but is strongly influenced by changes of the channel impedance.

It is, therefore, essential that device models treat TeraFETs as a whole—including the influence of high-frequency impedances of the integrated antenna as well as parasitic circuit elements—when simulations of the THz response are performed [34]–[36], [68], [69]. Naturally, this leads to different definitions of the detector *performance*, which will be addressed in detail further, depending on whether the intrinsic FET or the TeraFET device is the subject of the simulations.

For the simulation of a realistic TeraFET detector, we employ, here, a full device model introduced in parts for CMOS-based TeraFETs in previous papers [34], [36]. The propagation of the THz signal from the antenna to the gated channel region is treated with the equivalent-circuit representation of the TeraFET as shown in Fig. 1. We consider the case of *gate-drain coupling*, where the gate and the drain contacts are each connected with one arm of the integrated antenna (compare also the device design shown in Fig. 3). In addition, source and gate are ac-shorted by a shunt capacitor, which brings them onto the same ac potential. A plasma wave is then only injected into the channel from the drain side.

In AlGaN/GaN HEMT devices as well as in many other FET technologies except for Si-CMOS, the channel of the FET is usually only partially gated, and the gated region, where rectification takes place, is embedded in ungated access regions with gate-voltage-independent carrier density. At high frequencies, significant input power can be lost to these ungated channel segments. We describe them by the (real-valued) resistance $R_{\mathrm{ug}} = R_{\mathrm{ug,D}} + R_{\mathrm{ug,S}}$ and neglect any kinetic inductance assuming it to be small. Furthermore, we include the contact resistances in R_{ug} omitting a possible frequency dependence.

Considering the distribution of THz power from the antenna to the gated region of the TeraFET, two circuit elements are taken into account in the equivalent circuit of Fig. 1: the antenna impedance Z_{ant} and the resistances $R_{\mathrm{ug,S}}$ and $R_{\mathrm{ug,D}}$, which describe the ungated regions of the channel. Note that the capacitances between gate and source metallization and between gate and drain metallization—commonly denoted by $C_{\mathrm{gs-ext}}$ and C_{gd}, respectively—are part of the electromagnetic (EM) simulated structure in our analysis and thus absorbed in Z_{ext} and Z_{ant}, respectively. This differs from the case of Si-CMOS TeraFETs [34], [36], where the EM simulation does not consider transistor details and thus $C_{\mathrm{gs-ext}}$ and C_{gd} have to be included in the transistor model. We note that the measured classical transit frequency $f_{\mathrm{max}} \approx 80$ GHz of the GaN TeraFET is much lower than the frequencies for which plasma-wave-based detection is presented in the subsequent sections of this paper.

An important quantity, derived by harmonic analysis from the underlying hydrodynamic charge transport model [25], is the so-called *plasmonic efficiency factor* $f(\omega)$ describing the frequency-dependent enhancement of intrinsic self-mixing of the THz-induced plasma waves with respect to the quasi-static case of classical resistive self-mixing. For the gate-drain coupling situation in the GaN TeraFET presented in this paper (see Fig. 1), the efficiency factor takes the form as given in [34]. The THz-induced, intrinsic rectified photocurrent can then be expressed as the product of a quasi-static component I_{QS} and $f(\omega)$ as

$$I_{\mathrm{dev}} = I_{\mathrm{QS}} \cdot f(\omega) = \frac{q}{m} \frac{V_{\mathrm{a}}^2}{4s^2 R_{\mathrm{g}}} \cdot f(\omega) \qquad (1)$$

with R_{g} the dc resistance of the gated channel region. Here, ω and s are the angular frequency and phase velocity, respectively, of the plasma waves inside the channel. The constants q and m denote the elementary charge and the effective mass of charge carriers ($m = 0.2\, m_{\mathrm{e}}$ for electrons in Wurtzite GaN), and V_{a} is the amplitude of the THz oscillations at the drain side of the gated channel region.

At the same time, $P_{\mathrm{dev}} = (V_{\mathrm{a}}^2/2)\mathrm{Re}\{Z_{\mathrm{g}}^{-1}\}$ in general is only a fraction of the high-frequency power P_{in} arriving at the channel, while the residual power is dissipated in the ungated, drain-sided channel region [34], [69]

$$P_{\mathrm{dev}} = \left(\frac{\mathrm{Re}\{Z_{\mathrm{g}}\}}{\mathrm{Re}\{Z_{\mathrm{g}}\} + R_{\mathrm{ug,D}}} \right) \cdot P_{\mathrm{in}} = \mathbf{H} \cdot P_{\mathrm{in}} . \qquad (2)$$

The impedance Z_{g} of the gated channel region is again derived from harmonic analysis of the transport equations to be

$$Z_{\mathrm{g}} = \frac{iks^2 m}{\omega q^2 nW} \tan(kL_{\mathrm{g}}) \qquad (3)$$

for gate-drain coupling as first investigated in [34]. Here, k is the plasma wave's complex wave vector and n is the static gate-voltage-dependent carrier density. The gated channel width and length are denoted as W and L_g, respectively.

The important figures of merit to describe the performance of a detector are its responsivity (denoted as $\mathfrak{R}$) and its sensitivity, the latter expressed in terms of the NEP. The device current responsivity relates the rectified current I_{dev} to the power P_{dev} of the THz signal at the entrance of the gated channel region

$$\mathfrak{R}_{I,dev}(\omega) = \frac{I_{dev}}{P_{dev}} . \tag{4}$$

The term *device* serves as a reminder that the power considered here refers to the THz wave at the gated channel region and not that of the THz radiation impinging from free space onto the detector. The TeraFET's device NEP is defined accordingly as the ratio of the noise spectral density of the rectified signal (at dc or a low modulation frequency) to the device current responsivity $\mathfrak{R}_{I,dev}$. As TeraFETs are commonly operated at zero source–drain bias, it is fair to assume that only Johnson–Nyquist noise (thermal noise) of the dc resistance R_g is present [70]. In this case, one obtains

$$\mathrm{NEP}_{dev}(\omega) = \sqrt{\frac{4k_BT}{R_g}}\frac{1}{\mathfrak{R}_{I,dev}(\omega)} \tag{5}$$

with T being the device temperature (here: room temperature). Concerning the validity of the assumption of thermal noise, we have repeated earlier measurements on AlGaN/GaN TeraFETs [37] by new measurements in a noise lab at Vilnius University with a TeraFET of a recent fabrication run and similar in design to those investigated in this paper. The result is shown in the inset of Fig. 6 and once more confirms that no additional noise sources contribute significantly to the NEP of our AlGaN/GaN TeraFETs. Under certain circumstances, however, other noise sources, e.g., the influence of gate leakage currents, must be considered [71].

With regard to the rectified current, one has to take into account that the internal resistance of the gated channel limits the actual detected rectified current I_{det} as measured at the drain terminal of the TeraFET. Describing the rectification process in the form of a dc current source with an internal resistance R_g (see Fig. 1), we obtain for the detected dc photocurrent $I_{det} = I_{dev} \cdot \mathbf{H}_{DC}$ with

$$\mathbf{H}_{DC} = \frac{R_g}{R_g + R_{ug}} \tag{6}$$

with I_{dev} being the intrinsic, self-mixing-induced photocurrent in the gated channel by the available power P_{dev}. The responsivity referring to the power P_{in} at the drain side of the FET channel is then

$$\mathfrak{R}_{I,in} = \frac{I_{det}}{P_{in}} = \frac{I_{dev}}{P_{dev}} \cdot \mathbf{H}_{DC} \cdot \mathbf{H} = \mathfrak{R}_{I,dev} \cdot \mathbf{H}_{DC} \cdot \mathbf{H}. \tag{7}$$

For a full device picture of the TeraFET as a THz detector, the integrated antenna and optical coupling effects must be taken into account as well. This is accomplished by including the antenna impedance Z_{ant} and a coupling factor γ_{ant} into the device

model. The latter contains both the efficiency of coupling of the (Gaussian) THz beam to the antenna (hence, is a factor expressing the mode matching) and optical losses at the interfaces of a substrate lens as well as absorption losses in the lens and the substrate through which the radiation is transmitted (see Sections III and IV). Not yet included in γ_{ant} is any mismatch of the beam's cross section and the antenna cross section. This aspect is considered in the next paragraph. Values for Z_{ant} and antenna efficiency of our fabricated TeraFET were obtained from *S*-parameter simulations of the whole device structure including the antenna, the implemented metal-insulator-metal (MIM) capacitance Z_{ext}, and the stabilization environment[2] (see Section III and [35]) with a commercial Maxwell-solver software (CST Microwave Studio [72]).

In [59], we had already introduced the term *cross-sectional* responsivity. If the beam diameter is larger than the antenna cross section, only the amount P_c of the total beam power P_{THz} reaches the antenna (we use the subscript "c" for quantities related to the *cross section* of the integrated antenna). We obtain

$$P_{in} = \gamma_{ant} \cdot \mathbf{M} \cdot P_c$$
$$= \gamma_{ant} \cdot \frac{4 \left(\mathrm{Re}\{Z_g\} + R_{ug,D}\right) \cdot \mathrm{Re}\{Z_{ant}\}}{|Z_g + R_{ug,D} + Z_{ant}|^2} \cdot P_c \tag{8}$$

where we have introduced the antenna matching factor $\mathbf{M}$. The cross-sectional responsivity, referenced to P_c, is then given by

$$\mathfrak{R}_{I,c} = \frac{I_{det}}{P_c} = \frac{I_{QS}}{P_{dev}} \cdot f(\omega) \cdot \gamma_{ant} \cdot \mathbf{M} \cdot \mathbf{H}_{DC} \cdot \mathbf{H} \tag{9}$$

with

$$P_{dev} = \mathrm{Re}\left\{\frac{V_a^2}{2Z_g}\right\} = \frac{V_a^2}{2R_g} \cdot R_g\mathrm{Re}\left\{\frac{1}{Z_g}\right\}$$
$$= P_{QS} \cdot R_g\mathrm{Re}\{Z_g^{-1}\} \tag{10}$$

as

$$\mathfrak{R}_{I,c} = \mathfrak{R}_{I,QS} \cdot f(\omega) \cdot \gamma_{ant} \cdot \mathbf{M} \cdot \mathbf{H}_{DC} \cdot \mathbf{H} \cdot \mathbf{C} \tag{11}$$

using the identities

$$\mathfrak{R}_{I,QS} = \frac{I_{QS}}{P_{QS}}, \quad \mathbf{C} = \frac{1}{R_g\mathrm{Re}(Z_g^{-1})} \tag{12}$$

where $\mathbf{C}$ is the ratio of the gated channel admittances $1/R_g$ at dc and $\mathrm{Re}\{Z_g^{-1}\}$ at ac. It is worth noting that the majority of literature implicitly refers to cross-sectional responsivity (and NEP, respectively) when stating absolute numbers for detector performance of TeraFETs, and attention must be paid when comparing values between different publications.

Using (11) and the TeraFET's device parameters of Section IV, we calculated the expected cross-sectional responsivity $\mathfrak{R}_{I,c}$ and the corresponding NEP_c versus applied THz frequency. For the antenna coupling factor γ_{ant} we obtained a value of ~ 0.1 from the simulated antenna efficiency and a Gaussian coupling efficiency of $\sim 60\%$ including optical losses of $\sim 30\%$ [73]. The results are shown in Fig. 2 for the gate bias values, which

---

[2]An additional capacitance of 1 fF was added in parallel to the antenna, accounting for the finite port impedance intrinsic to the numerical solver software.
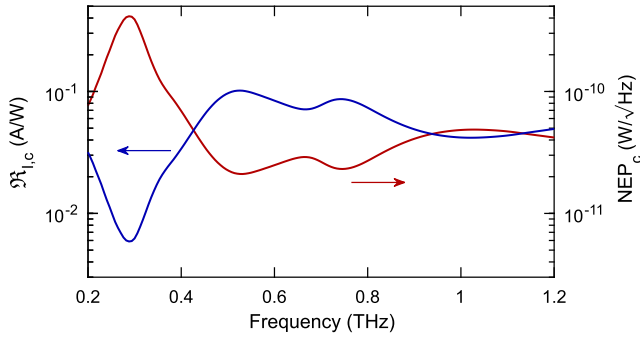
Fig. 2. Simulated cross-sectional responsivity $\Re_{I,c}$ ($V_G = -1.0$ V, blue curve, left axis) and cross-sectional NEP$_c$ ($V_G = -1.1$ V, red curve, right axis) as a function of radiation frequency for a TeraFET with gate-drain THz coupling and gate-source ac shunting, and for device parameters as determined for the fabricated GaN TeraFET (see Sections III and IV).
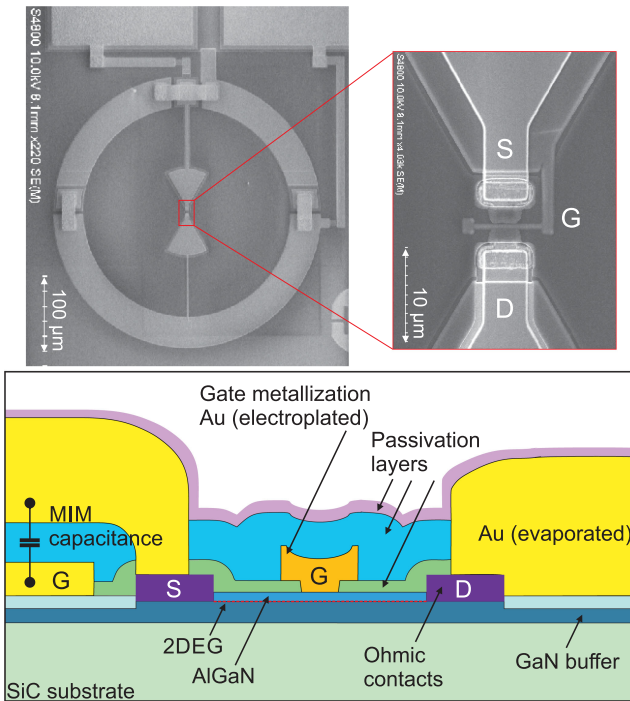

Fig. 3. Top: SEM images of the TeraFET. The magnification shows the active transistor region. The overlay of the gate and source antenna wings forming the MIM capacitance can be seen. Bottom: Schematic cross-sectional view of the AlGaN/GaN TeraFET.

yield the minimum NEP$_c$ ($V_G = -1.1$ V) and maximum device responsivity ($V_G = -1.0$ V). At 0.52 THz, we find a minimum NEP$_c$ of 21 pW/$\sqrt{\text{Hz}}$ corresponding to a maximum $\Re_{I,c}$ of 102 mA/W at the same frequency. At low frequencies, the simulations produce a pronounced resonance (a dip in the responsivity and a peak in NEP$_c$) around 0.3 THz, which can be attributed to a metal ground ring of the detector environment (see detector design in Fig. 3). At this frequency range, the ring itself acts as an additional resonant antenna structure, and the incident THz beam is not properly coupled to the integrated bow-tie antenna. The feature shows up in our simulation because the antenna S-parameters were simulated for the entire detector

structure including the stabilization environment[3] and is also reproduced in the experimental data (see Fig. 7, Section VI).

To summarize this section, the design of efficient TeraFETs requires a detailed modeling of the power coupling between the integrated antenna and the intrinsic rectifying detector element. The design goal should be the reduction of parasitic impedances as well as impedance matching of the integrated antenna to ensure maximum power coupling to the gated region of the FET's channel. In our design work discussed in Section III, we chose the approach to achieve high detection sensitivity (low NEP) of our TeraFETs by getting as close as possible to impedance matching for the long-channel approximation of the nonresonant plasma-wave-based detection principle. This was motivated by our target to develop a broadband detector with rather constant $\Re_{I,c}$ and NEP$_c$ values over a frequency range as large as possible starting at 0.4 THz.

III. TeraFET Design and Fabrication

We present here an improved generation of broadband Al-GaN/GaN TeraFETs, which we designed and fabricated on the basis of previous characterization experiments [35], [51], [59] as well as thorough simulation of the plasma-wave-based mixing mechanism and the device model presented in Section II. The improved detector design combines optimization of the intrinsic THz rectification as well as stabilization of the RF environment and reduction of parasitic influences. For fabrication of the optimized TeraFETs, we employed a 100-nm GaN MMIC process recently developed at Ferdinand-Braun-Institut, Leibniz-Institut für Höchstfrequenztechnik (FBH) Berlin with a reduced gate-to-channel separation of $d = 12$ nm of the AlGaN/GaN HEMTs. Fig. 3 shows micrographs and a schematic cross-sectional view of the device. The transistor's channel length L is given by the length of the gated channel region of $L_g = 100$ nm and of two ungated (access) regions of 300 nm each. We chose the channel width to be $W = 3$ μm based on previous investigations [47]. A semi-insulating, THz-transparent silicon carbide substrate with a thickness of 470 μm was used for the epitaxial growth of the AlGaN/GaN layers. This allows coupling of the THz radiation through the substrate with a substrate lens (see Section V). The epitaxial structure has an Al$_{0.32}$Ga$_{0.68}$N barrier with a resulting 2DEG sheet resistance of r$_s$ = 610 Ω/sq, the specific resistance of the ohmic contacts amounts to r$_c$ = 0.8 $\Omega \times$ mm. The design of the THz detector includes a bow-tie-type broadband antenna, with an opening angle of $\alpha = 60°$ and a single-wing length of $l = 60$ μm, fabricated by evaporation of a 650-nm-thick gold layer. S-parameter simulations of the bow-tie antenna including the surrounding structures yielded a reasonably flat impedance of around 100 Ω between 0.45 and 1.2 THz. One of the antenna wings is realized as an MIM capacitor between source and gate with a 200-nm-thick dielectric separation layer of SiN$_x$. The capacitance is designed to act as a high-frequency shunt for the incoming THz radiation to ensure asymmetric power coupling into the channel from the drain side only—the asymmetry being

---

[3]This responsivity dip was not a design flaw because the TeraFETs were planned as broadband detectors for frequencies of 0.4 THz and higher, i.e., beyond this parasitic resonance frequency.
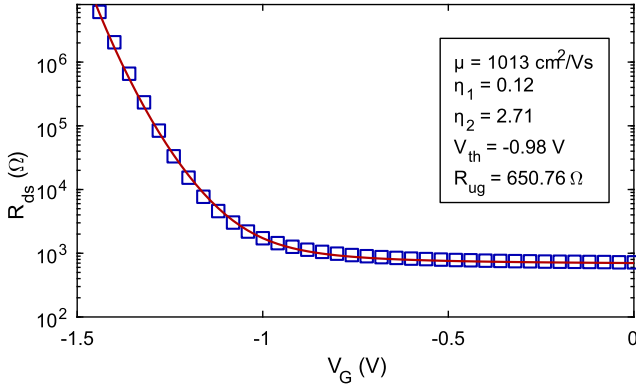
Fig. 4. Fit (red line) of the TeraFET's measured dc drain–source resistance $R_{\rm ds}$ (blue squares) with a drift-diffusion model based on (13).

a crucial condition for efficient plasma wave rectification [16], [25], [34], [51]. The gate-source MIM design can be seen in the magnified SEM image in Fig. 3. The rectified signal is read out as a dc current or voltage from the drain port.

Besides optimization of the active detector elements, we implemented stabilization measures in the detector's environment for ac and dc decoupling. For instance, a ground ring, which can be seen in the SEM image in Fig. 3, is used for ac decoupling from neighboring detector structures. Recall that around 0.3 THz this ground ring is responsible for a strong decrease of the antenna impedance leading to a large mismatch to the FET channel, which manifests in a dip in the simulated (see Fig. 2) and measured (see Fig. 7) responsivity, and a peak in the NEP, respectively. Some further details on the stabilization environment can be found in the work presented in [35].

IV. DC PARAMETER EXTRACTION

In Section II, we discussed that the THz response of TeraFETs can be modeled by hydrodynamic transport theory describing the intrinsic detection mechanism and by taking the high-frequency impedances of intrinsic and extrinsic device components into account. A key step of real device modeling is the extraction of the fundamental physical device parameters of the TeraFETs, such as the carrier mobility and the total resistance of the ungated channel regions (including contact resistances). We performed parameter extraction by analyzing the dc drain–source resistance $R_{\rm ds}$ by a two-stage fit routine, where we deduced the resistance from dc conductance measurements taken at a low source–drain voltage of 10 mV. Fig. 4 shows the experimental data together with the fitted curve. The fit model was developed based on a description of the gate-voltage-dependent carrier density in the gated channel region of the HEMT derived from the unified charge-density control model[4] of [75] as

$$n(V_{\rm G}) = \frac{C_{\rm gc}\eta(V_{\rm G})V_{\rm T}}{q} \ln\left(1 + \frac{1}{2}\exp\left(\frac{V_{\rm G} - V_{\rm th}}{\eta(V_{\rm G})V_{\rm T}}\right)\right) \quad (13)$$

[4]We note that alternative approaches to physics-based charge control models for AlGaN/GaN or GaAs HEMTs have been proposed [74].

with the nonideality factor

$$\eta(V_{\rm G}) = 1 + \ln\left(1 + \exp\left(\eta_1\left(\frac{V_{\rm G} - V_{\rm th}}{V_{\rm T}}\right) + \eta_2\right)\right). \quad (14)$$

Unlike in the case of other material systems such as Si CMOS, $\eta(V_{\rm G})$ is no longer a constant, but itself depends on the applied gate voltage $V_{\rm G}$. Here, $C_{\rm gc} = \varepsilon_0\varepsilon_{\rm r}/d$ is the geometric gate-to-channel capacitance per unit area, $V_{\rm T} = k_{\rm B}T/q$ the thermal voltage at room temperature ($T = 294$ K), and $V_{\rm th}$ the transistor threshold voltage.

In the first stage of the routine, we fitted the inverse of the measured dc resistance $R_{\rm ds}$ in the strong-inversion regime ($V_{\rm G}$ far above threshold), where (13) can be linearized to

$$n(V_{\rm G}) = \frac{C_{\rm gc}(V_{\rm G} - V_{\rm th})}{q}. \quad (15)$$

The total channel resistance $R_{\rm ds}$ is divided into a gate-voltage-dependent part $R_{\rm g} \propto 1/n$ plus a constant value $R_{\rm ug}$ containing both the ohmic contacts as well as the ungated channel regions.[5] The threshold voltage $V_{\rm th}$ is also extracted from this fit via (15). In the second step, the measured $R_{\rm ds}$ is fitted over the whole range of gate voltages $V_{\rm G}$ based on a dc drift-diffusion model [76]. Here, the dc conductivity of the gated channel region is represented as the sum of a drift term $\sigma_{\rm drift} = qn\mu$ and a diffusive term $\sigma_{\rm diff} = q\mu V_{\rm T}(\partial n/\partial V_{\rm G})$ with n according to (13). For the device presented in this paper, we find the parameters $V_{\rm th} = -0.98$ V, $R_{\rm ug} = 650.76$ Ω, and the charge carrier mobility $\mu = 1013$ cm^{2}V^{-1}s^{-1} yielding an electron momentum scattering time $\tau_{\rm p} \sim 115$ fs in addition to the two dimensionless parameters $\eta_1 = 0.12$ and $\eta_2 = 2.71$. For the term $R_{\rm ug,D}$ in the equations for the responsivities in Section II, we used $R_{\rm ug,D} = R_{\rm ug}/2$ due to the symmetric layout of the AlGaN/GaN HEMT.

V. EXPERIMENTAL SETUP FOR TERAFET CHARACTERIZATION

We experimentally characterized our AlGaN/GaN TeraFETs with two seperate setups, all measurements were performed at room temperature. The top of Fig. 5 shows a schematic of the TeraFET characterization setups. Both employed a combination of two polytetrafluoroethylene (PTFE, Teflon) THz lenses for collimation and prefocusing of the THz beam. The first setup employed a tunable multiplier-chain-based all-electronic source working from 490 to 645 GHz. The available continuous-wave THz beam power was recorded with a calibrated large-area photo-acoustic power meter [77] and allowed for absolute NEP measurements in this frequency range. The system yielded a THz power of around 50 μW at the position of the TeraFET detector module behind the two PTFE lenses (power spectra not shown). The second setup used a broadband photomixer-based THz source (Toptica Terascan 1550 [78]) using two temperature-tuned distributed feedback (DFB) fiber lasers with 1550-nm center wavelength [79], and a substrate-lens-coupled photoconductive antenna on InGaAs. The system can be tuned over a broad

[5]From the device dimensions together with the values of the 2DEG sheet resistance $r_{\rm s}$ and the specific contact resistance $r_{\rm c}$ given in Section III, a gate-voltage-independent resistance $R_{\rm ug} = 656$ Ω is expected, which is well reproduced by the fit model.
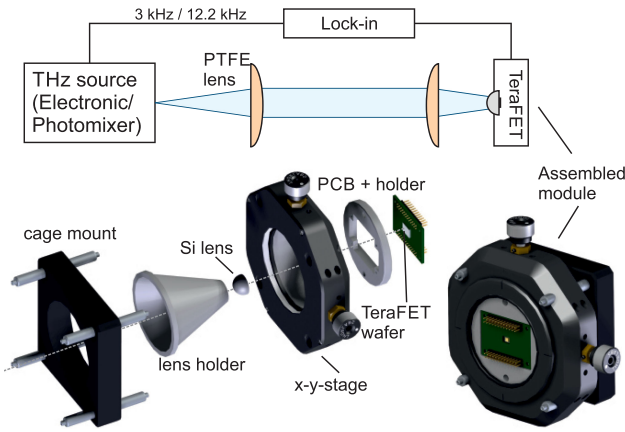
Fig. 5.   Top: Experimental setup for THz characterization of the TeraFETs with an electronic source for calibrated measurements and a photomixer source for broadband ones. Bottom: Drawing of the TeraFET detector module as used in the characterization experiments. The dashed line represents the optical axis of the setup with the THz beam illuminating the TeraFET from the left through the substrate lens.

frequency range and TeraFET characterization with this setup was performed from 0.2 to 1.2 THz. The available THz power was significantly lower compared to that of the electronic source ($< 4\ \mu$W at 500 GHz and decreasing exponentially with rising radiation frequency). Thus, absolute THz power measurements were not possible with the calibrated power meter because of its sensitivity limitation. As an alternative, we decided to perform comparative measurements with two other types of broadband THz detectors. We chose to compare our TeraFETs' broadband signal-to-noise ratio (SNR) with those obtained with two commercial detectors—namely, the THz photomixing detector of the Toptica Terascan 1550 and a Golay cell detector.

Since the directivity of planar antennas on substrates is mainly oriented into the substrate, we illuminated our detectors through the SiC substrate using a silicon lens to focus the THz beam tightly onto the TeraFET antenna. We chose a hyper-hemispherical lens shape (radius 6 mm, extension length 1.2 mm including the thickness of the SiC substrate) to reach an aplanatic optical configuration, where internal reflections inside the substrate lens are eliminated [73], [80]. For this geometry, we estimate a Gaussicity of 88%. The lower part of Fig. 5 shows a technical sketch of the TeraFET measurement module. The silicon lens is held in place on the optical axis of the setup by a conical tube, while the wafer die containing the TeraFET—glued and wire-bonded to a PCB read-out board—is mounted on an *x-y* stage to allow for precise positioning with respect to the fixed silicon lens (this also facilitates switching between multiple detectors on a single die). During the measurements, the THz sources were chopped electronically at a modulation frequency of 3.3 kHz for the electronic source and 12.2 kHz for the photomixer source, respectively. A lock-in amplifier was used to detect the voltage or current response of the TeraFET.

At this point, we want to address again the issue of power referencing of the detected dc current signal I_{det}. For the presentation of the values of a TeraFET's NEP and responsivity, a precise specification of the THz power used in the calculation is essential for a meaningful determination of detector

performance and for comparison with other detectors. As stated earlier, we distinguish the *optical* NEP and responsivity, the *cross-sectional* NEP and responsivity, and the *device* NEP and responsivity, denoted as NEP_{opt} and $\mathfrak{R}_{\text{I,opt}}$, NEP_{c} and $\mathfrak{R}_{\text{I,c}}$, and NEP_{dev} and $\mathfrak{R}_{\text{I,dev}}$, respectively. The first refers to the total available THz beam power P_{THz} measured at the position of the detector module in front of the substrate lens, while the second one refers to the power reaching the detector's antenna cross section and is the key quantity of our simulations [see (11)]. The third one refers to the power P_{dev} reaching the TeraFET's gated channel region and is available to the intrinsic rectification process. From an experimental point of view, the latter two powers are not readily accessible and require some effort to be determined [19], [81]. This process can be critical and unfortunately is not always transparently described in the literature, which makes the comparison of detectors difficult on the basis of literature data only. Furthermore, values of device NEPs and responsivities are usually of only limited use and reliability, if one aims at the development of a detector module. For these reasons, all experimental NEP values in this paper are *optical* NEP values referring to the total THz beam power P_{THz} as measured with the large-area power meter at the position of the TeraFET module, i.e., after the two PTFE lenses. The NEP_{opt} values are never smaller than the NEP_{c} values, and $\mathfrak{R}_{\text{I,opt}}$ is never larger than $\mathfrak{R}_{\text{I,c}}$, the *optical* quantities hence provide a conservative approximation of a detector's performance. Accordingly, in Section VI, we will compare our detectors with other detectors for which the respective literature provides optical NEP values.

VI. TeraFET Characterization Results

In this section, we present the results of the experimental THz characterization of our TeraFETs and compare their performance with the simulated data as well as other state-of-the-art, broadband THz detectors from the literature. In a first measurement, we determined the optimum bias point of detector operation, i.e., the gate voltage where the detector's sensitivity is highest, corresponding to a minimum of NEP_{opt}. For this purpose, we performed measurements of the gate-voltage-dependent THz responsivity $\mathfrak{R}_{\text{I,opt}}$ with the electronic THz source at 504 GHz. The result is shown as blue curve in the main panel of Fig. 6. We point out again that in this setup, the measurement gives absolute values since the THz power P_{THz} could be measured with the calibrated power meter capturing the entire cross section of the THz beam. The optical current responsivity is then given by

$$\mathfrak{R}_{\text{I,opt}} = \frac{\pi}{\sqrt{2}} \frac{I_{\text{det}}}{P_{\text{THz}}}. \qquad (16)$$

Since the radiation source was square-wave modulated at 3.3 kHz for lock-in detection, a factor of $\pi/\sqrt{2}$ must be included in the calculation. From these data, together with the measured dc drain–source resistance R_{ds} (see Fig. 4), we calculated the optical NEP of the TeraFET according to [compare (5)]

$$\text{NEP}_{\text{opt}} = \sqrt{\frac{4k_{\text{B}}T}{R_{\text{ds}}}} \frac{1}{\mathfrak{R}_{\text{I,opt}}}. \qquad (17)$$
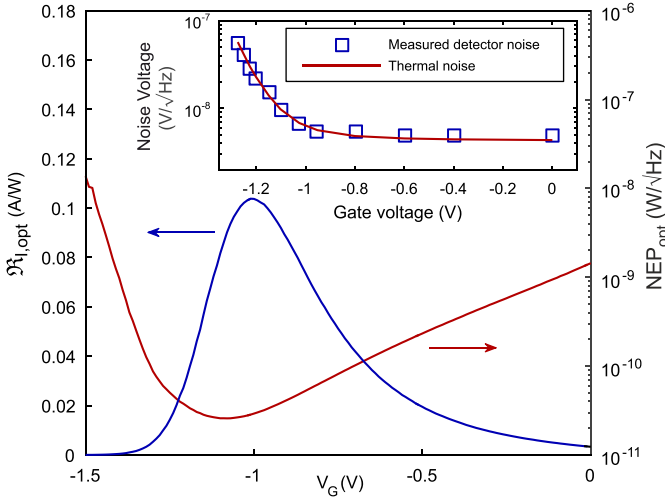
Fig. 6. Measured optical current responsivity $\Re_{I,opt}$ (blue curve, left axis) and optical NEP_{opt} (red curve, right axis) of the TeraFET at 504 GHz as a function of gate voltage. The maximum value of $\Re_{I,opt}$ is 104 mA/W at $V_G = -1.01$ V, and the minimum value of NEP_{opt} is 26 pW/$\sqrt{Hz}$ at $V_G = -1.09$ V. Inset: Measured detector noise voltage (different device of the same design) compared to thermal noise voltage calculated from the measured R_{ds}.
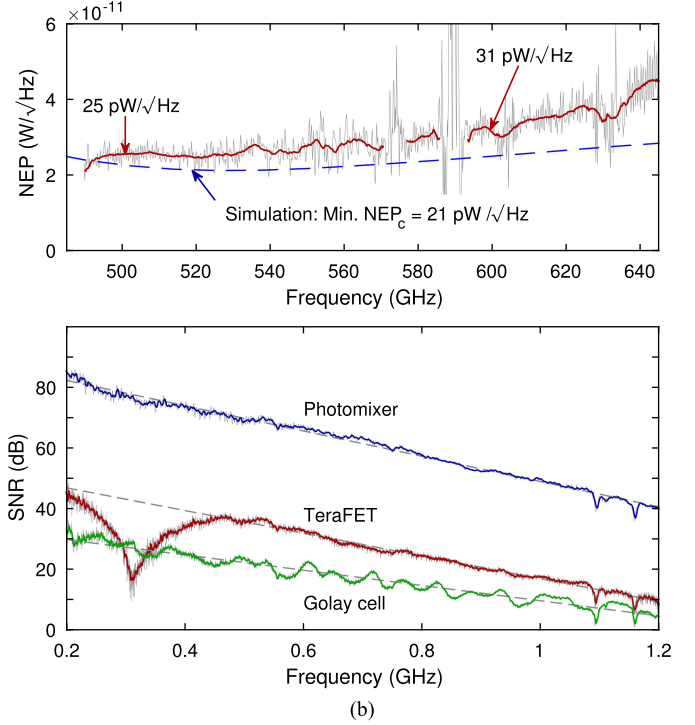

(b)

Fig. 7. (a) Optical NEP (gray curve, raw data) of the TeraFET measured with the all-electronic THz source between 490 and 645 GHz, and simulated cross-sectional NEP_c (blue dashed line) extracted from Fig. 2. The red solid line was obtained applying a moving average filter to smooth out standing-wave oscillations (the gap regions were ignored in the smoothing due to a lack of THz source power in these ranges). (b) Comparison of the SNR of three THz detectors—a photomixer, our TeraFET, and a Golay cell. Raw data given in gray for all measurements, smoothed data as colored solid lines as in (a), dashed lines denote linear regressions.

The result is plotted as a red curve in the main panel of Fig. 6. Note that the gate bias points of maximum responsivity and minimum NEP, as usual, do not coincide, as already observed in the simulations in Section II. From the experimental data, we find an optimum gate bias point of $V_G = -1.09$ V for NEP_{opt} corresponding to a drain–source resistance of $R_{ds} = 7.6$ kΩ.

We note that in a setup as employed here, standing waves can develop, in particular, at lower THz frequencies. This can lead to an overestimation of the detector sensitivity, since usually the setup is aligned to yield a maximum detection signal, which is more likely to be obtained for constructive interference conditions. A strong reduction of standing waves can be achieved by placing THz attenuators in the beam path, however, such an option is not practical when working with low-power THz sources. Alternatively, one can compensate the standing-wave effect by spatial, spectral, or phase scans and by then taking the average over at least one period of the interference patterns. While this was not done for the single-frequency measurement of Fig. 6, the experiments discussed in the following used spectral scanning with a frequency resolution of 0.1 GHz allowing for an averaging of the standing wave oscillations.

Fig. 7(a) shows results of slow-spectral-sweep measurements of the detector response evaluated in terms of the optical NEP in the frequency range from 490 to 645 GHz. The radiation source was the all-electronic THz emitter. The light gray curve displays the raw data exhibiting standing waves as explained before. The overlayed thick red line was obtained by passing an averaging filter over the raw data; where the line is interrupted, no reliable THz signal could be measured due to the low source power. The sweep was performed at the fixed gate bias voltage of $V_G = -1.09$ V previously determined as best bias point. We observe a continuous increase of NEP_{opt} with frequency in the investigated spectral region, with values of 25 and 31 pW/$\sqrt{Hz}$ at

504 and 600 GHz, respectively. The performance of the investigated TeraFET represents an improvement of more than a factor of two compared to our previous devices [35]. To the best of our knowledge, these optical NEP values constitute record values for the optical sensitivity of AlGaN/GaN HEMT-based TeraFET detectors in this frequency region. Table I presents the achieved absolute optical sensitivity of the TeraFETs of this work together with a number of different—in part commercially available—THz detectors for broadband operation, and also shows a number of resonant (or small-bandwidth) detector implementations for comparison.

We now come to the comparison of the measurement results with those of the simulations. Fig. 7(a) includes simulation data for NEP_c already presented in Fig. 2. At 500 and 600 GHz, the NEP_c values are 22 and 25 pW/$\sqrt{Hz}$, respectively. Measurement and simulation show a good qualitative agreement over the frequency range covered in Fig. 7(a), with an offset of the measured data, which is expected to arise at least to a certain degree from the fact that not all power of the THz beam couples to the detector's antenna cross section. The good agreement between measured NEP_{opt} and calculated NEP_c give the simulations from Section II considerable credibility.

The TeraFET was further characterized with the broadband photomixer system between 0.2 and 1.2 THz. The absolute THz

TABLE I
ABSOLUTE OPTICAL SENSITIVITES OF VARIOUS BROADBAND AND RESONANT, ROOM TEMPERATURE THz DETECTORS

Detector type/ technology	Optical NEP (pW/$\sqrt{\text{Hz}}$)	Working frequency	Reference	Comments
Broadband detectors				
Golay cell	$100 - 1000$	$\geq 30\,\text{GHz}$	[82]	commercial
Pyroelectric	~ 400	$\geq 30\,\text{GHz}$	LiTaO$_3$, [83]	commercial
Photoacoustic powermeter	$\sim 5 \times 10^6$	$\geq 30\,\text{GHz}$	[77]	commercial
Microbolometer (VO$_x$)	14.4	2.5, 4.2 THz	[2]	single-frequency measurement
Microbolometer (Si)	6	2.5 THz	[3]	single-frequency measurement
Hot-electron bolometer	5000	2.55 THz	[84]	single-frequency measurement
SBD	7-100	0.15 - 1 THz	[85]	also commercial, e.g., [86]
zero-bias SBD	45-115	0.1 - 1 THz	[87]	commercial
TeraFET (AlGaN/GaN HEMT)	25 - 31	$0.49 - 0.65\,\text{THz}$	this work	
TeraFET (AlGaN/GaN HEMT)	30-50	$0.7 - 0.9\,\text{THz}$	[53]	power referencing not clear
TeraFET (65-nm Si-CMOS)	100	$0.8 - 1\,\text{THz}$	[33]	
TeraFET (90-nm Si-CMOS)	48-70	$0.6 - 1.5\,\text{THz}$	[36]	
TeraFET (graphene FET)	515	0.6 THz	[41]	single-frequency measurement
Thermopile	1000	1.63, 2.52, 4.25 THz	[88]	single-frequency measurement
Sb-HBD	850	$0.6 - 1\,\text{THz}$	[10]	
Resonant detectors				
TeraFET (90-nm Si-CMOS)	20, 63, 85, 110, 404	0.59, 2.52,3.11,4.25, 4.75 THz	[20], [37], [89]	
TeraFET (65-nm SOI-CMOS)	17	0.65	[90]	
TeraFET (65-nm Si-CMOS)	14	0.72	[39]	calculated (ideal antenna aperture)
130-nm SiGe BiCMOS	8.4	0.26	[91]	
SiGe-HBT	30	0.645	[92]	
SiGe-HBD	11	0.17	[93]	calculated from optical losses
SBD (130-nm CMOS)	5000	4.92	[94]	
SBD (GaAs)	330	2.54	[95]	
zero-bias SBD	1.1, 1.3, 2.1	0.09-0.14, 0.17-0.26, 0.26-0.4	[87]	commercial, waveguide-coupled
BiSb Thermocouple	170	0.812	[96]	

For a comparison of Si-based technologies, also see [22].

power of the photomixer source could not be measured over this broad frequency range. Therefore, instead of absolute NEP values, we calculate the detector's SNR as the ratio of detected current signal I_{det} and current noise N_I

$$\text{SNR} = \frac{I_{\text{det}}}{N_I} \tag{18}$$

where again, for the TeraFET, we use only thermal noise contribution. The measured SNR is plotted as a gray curve in Fig. 7(b) (red curve: sliding average). The measurement was performed at a modulation frequency of 12.2 kHz with a lock-in time constant of 100 ms. We find a nearly linear decrease of the TeraFET's SNR versus frequency in the dB-scale graph. The decay is mainly attributed to the exponential decrease of the available output power of the THz source. We observe a strong dip of the SNR at around 300 GHz, similar to the dip in the responsivity simulation of Fig. 2 in Section II. As discussed earlier, we attribute this feature to an interaction of the bow-tie antenna with the surrounding ground ring (see Fig. 3). This assumption was further corroborated when we characterized TeraFETs with

bow-tie antennas but without a ground ring (data not shown here).

Finally, we compare the performance of our TeraFET in terms of SNR to two commercially available broadband THz detectors. First, we used a photoconductive-antenna-based detector equivalent to the transmitter of the tunable THz system (see Section V). The induced photocurrent was measured in the usual coherent mode of an optoelectronic THz measurement system. The plot in Fig. 7 (blue curve) shows the extracted amplitude envelope of the phase-sensitive sweep measurement performed again at a modulation frequency of 12.2 kHz and a time constant of 100 ms. Again, we find a near-linear frequency dependence in the dB-scale graph with comparable slope (~ 0.04 dB/GHz from linear regression, dashed lines). The SNR of the photomixer is more than 30 dB higher than that of the TeraFET. This is not surprising, since the TeraFET detector works as a direct power detector [25], while the photomixer represents a coherent detector and enjoys a much better noise suppression by the phase-sensitive detection. It should be mentioned, however, that TeraFETs can also be operated in a coherent way, e.g., as heterodyne detectors, for which it was shown that application of
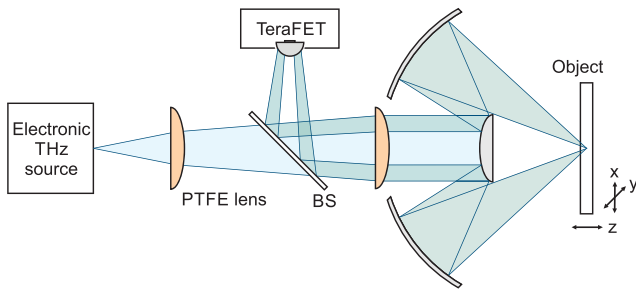
Fig. 8. Schematic of the imaging setup for reflection (not to scale). The THz source illuminates the object through a Schwarzschild telescopic mirror objective, the beam reflected from the object-under-test returns along the same beam path and is guided to the TeraFET with the help of a silicon beamsplitter. The object is scanned across the focal spot of the objective.
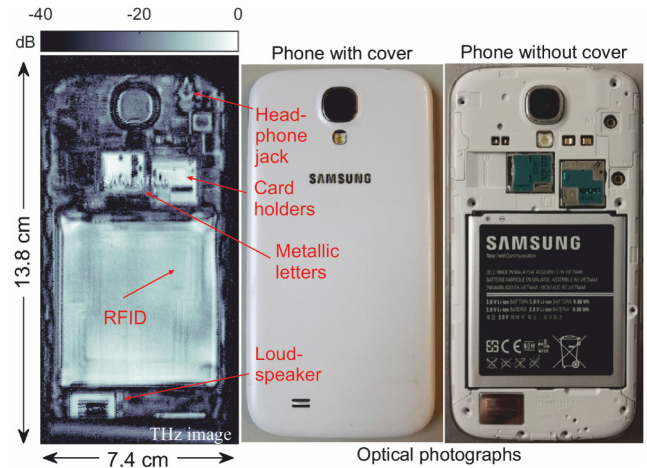

Fig. 9. Left: THz reflection image of a cell phone at 504 GHz. The image was recorded through the back cover of the phone, with the phone as shown in the photograph in the middle. The photograph on the right shows the interior of the phone with the back cover removed. Features such as the loudspeaker, the metal holders for SIM and memory card, various semiconductor chips as well as the headphone jack (invisible in the optical image) can be identified in the THz image. Furthermore, an optically invisible RFID loop antenna can be seen to be embedded under the cover of the phone's battery. The overall dynamic range of the image exceeds 40 dB.

an even low local-oscillator powers can be sufficient to improve the SNR by approximately 25 dB [27]–[29].

Finally, we used the same setup to measure the SNR of a commercial Golay cell detector. Due to the low THz power, lock-in measurements at a time constant of 100 ms were not possible, instead, measurements were performed with a lock-in time constant of 2 s. We determined the noise voltage of the Golay cell to be $N_V \approx 17.5 \, \mu\text{V}/\sqrt{\text{Hz}}$ (for voltage read-out) and then calculated the corresponding SNR for a 100-ms integration time based on the equivalent noise bandwidth for the given filter slope setting of the lock-in amplifier. The data are shown as a green curve in the lower panel of Fig. 7. The TeraFET exceeds the dynamic range of the Golay cell by roughly 20 dB for frequencies above 0.4 THz. The overall frequency dependence is slightly less steep than that for the other two detectors (0.03 dB from linear regression). However, the SNR curve of the Golay cell is overlayed with a pronounced modulation over the whole frequency range, attributed to strong etalon resonances in the cell's diamond window and the active gas-filled cavity.

VII. REFLECTION IMAGING

In order to demonstrate the high dynamic range of the TeraFETs, we used the device, whose characterization was described in Section VI, for reflection-mode imaging. A schematic drawing of the imaging setup is depicted in Fig. 8. A Schwarzschild telescope objective was employed as optical element, which permits tight focusing because of its large numerical aperture. It consists of two spherical mirrors—a convex reflector and a concave one—in a monocentric configuration. The telescope was built in-house. The spherical reflecting surfaces are relatively easy to fabricate in a mechanical workshop by cutting the mirror-shapes into blocks of aluminum; a surface quality sufficient for THz radiation can be readily achieved. The objective is free from spherical and chromatic aberrations [97], which in particular is of high value for multispectral imaging applications. The telescope has an effective focal length of $f = 50$ mm and a numerical aperture of NA = 0.67. Two PTFE lenses were used for precollimation and prefocusing of the incident and the reflected THz beam, respectively, to ensure nearly the same beam coupling conditions as in the TeraFET characterization setup (see Fig. 5). The object to be imaged was

raster-scanned across the focused THz beam with the help of mechanical translation stages.

The test object was a commercial cell phone, shown in the two photographs on the right side of Fig. 9. THz images were taken of the backside of the closed phone (in the state as shown in the photograph in the middle of Fig. 9). The image on the left side displays a THz reflection image recorded at 504 GHz. As the THz radiation penetrated the plastic cover of the phone as well as other plastic components within, the internal reflective structure of the phone was recorded. Given the large NA of the Schwarzschild objective, one can perform depth-resolved imaging. We recorded a number of depth-slice images by translating the object along the *z*-direction (steps of 250 μm) and chose the *z* plane where the internal features of the phone became most clearly visible and sharp. The reflection images were acquired with a step size of 400 μm in *x*- and *y*-direction at a scan speed of 15 mm/s for the fast (*x*-)axis; the lock-in integration time was 20 ms. The total image acquisition time was 40 min.

Details of the phone's interior can be recognized in the THz image—this being mainly highly reflective metallic and semiconductor-chip structures. The metallic cover of a loudspeaker as well as the metal holders for SIM and memory card above the battery is visible. In the top right corner, the headphone jack can clearly be seen, which is invisible even in the optical photograph with the back cover removed (right image in Fig. 9) because it is concealed by another plastic layer. Another feature invisible in the optical photograph but unveiled in the THz reflection image are several windings of an RFID loop antenna on the back of the phone's battery, which is covered by a visually opaque layer of black foil. Finally, the manufacturer's logo engraved in metal letters on the surface of the phone's plastic cover (and appearing black in the photograph in the middle of Fig. 9)

can be recognized in the THz reflection image, although the letters there are strongly blurred, since the depth layer was about 1.5 mm shifted from the focal plane of the reflection objective.

Similar to the TeraFET characterization setup shown in Fig. 5, the reflection imaging setup exhibits standing waves. When the object to be raster-scanned has height variations or—if the surface is perfectly flat—is slightly tilted with respect to the optical axis of the imaging system, the effect becomes visible as interference pattern in the recorded intensity image. The intensity variations visible in the THz image on the phone's battery are most likely caused by such standing waves. A way to avoid this effect would be the tuning of the THz frequency and overlaying multiple scans to average out the interferences, however, at the cost of increased image acquisition time.

VIII. Summary and Conclusion

In conclusion, we have presented our recent development of sensitive broadband THz detectors based on field-effect transistors with integrated antennas (TeraFETs). Careful design and thorough simulations led to the implementation of optimized AlGaN/GaN TeraFETs with a more than twice enhanced sensitivity compared to the previous works on TeraFETs in the AlGaN/GaN material system [35], [51], [59], slightly better even than broadband Si CMOS TeraFETs [36], and with a performance almost comparable to that of state-of-the-art Schottky-diode-based detectors around 0.6 THz, however, without the significant roll off toward higher frequencies typical for Schottky detectors [8].

The presented simulations were based on a hydrodynamic transport model for the description of the rectification process in the gated transistor region included in a full-device model considering also extrinsic effects by the impedances of the transistor's access regions and the antenna, as well as the antenna efficiency and optical coupling losses. Fundamental device parameters were extracted from the measured dc drain–source resistance curve with a fit routine based on a drift-diffusion model and a charge-control equation, which was refined by us for AlGaN/GaN HEMTs. We showed that with a reasonable estimate of optical and antenna-coupling losses, we could predict the measured optical NEP values remarkably well. The simulations predicted values of the cross-sectional NEP_c (which can be compared with the optical NEP except for the mismatch of the beam and antenna cross section) of 22 and 25 pW/$\sqrt{Hz}$ at 500 and 600 GHz, respectively.

We note that the simulations neglected rectification contributions by the hot-carrier thermoelectric effect. While it is known that it contributes in our devices, the degree of its importance cannot be specified at this time.[6] Simulations based on a more complete charge and energy transport model [76] are under way. Another direction of work is the investigation of THz detection with AlGaN/GaN TeraFETs over an extended frequency range up to several THz.

Two methods for the characterization of the TeraFETs were applied: 1) Absolute NEP measurements with an all-electronic source in the frequency range between 490 and 645 GHz, where we measured record values of the optical NEP of 25 and 31 pW/$\sqrt{Hz}$ at 500 and 600 GHz, respectively. 2) A direct comparison of the broadband SNR of our device with two commercial room-temperature THz detectors—a Golay-cell power detector and a coherent photomixer. In terms of maximum SNR, the coherent photomixer outperformed the two direct power detectors as expected, but the AlGaN/GaN TeraFET exceeded the SNR of the Golay cell by roughly 20 dB. In terms of frequency dependence, we obtained a slightly flatter response of the TeraFET than the photomixer system, both systems incorporating integrated bow-tie antenna structures. With the presented performance, we believe that GaN TeraFETs are now competitive to SBDs as the state-of-the-art of semiconductor-based THz detectors and can in the future play an important role in possible applications of THz technology.

Finally, we demonstrated the capabilities of our GaN TeraFETs for high-dynamic-range reflection imaging. A Schwarzschild optics was employed to record a THz image through the plastics cover of a commercial cell phone at 504 GHz, yielding a dynamic range of >40 dB and unveiling a number of visually hidden features. The image acquisition required a rather long time of 40 min. Here, TeraFETs offer the potential of fabrication of focal-plane arrays with high yield, which has been demonstrated before, e.g., in [20] and [33]. We are currently working on the implementation of a broadband 12×12 pixel focal plane array employing the same AlGaN/GaN TeraFETs as presented in this paper.

Acknowledgements

<hr>

⁶Thermoelectric signals in TeraFETs are not included in the transport model in this work. An extension of the reduced transport model from [25] to an energy transport model is required [76]. We reported on this topic previously on the basis of clear experimental evidence [41], [59], [60], [98]. We have implemented a comprehensive device model for THz rectification in TeraFET and will discuss thermoelectric currents in TeraFETs in detail elsewhere.

References

[1] N. Oda, "Uncooled bolometer-type terahertz focal plane array and camera for real-time imaging," *C. R. Phys.*, vol. 11, no. 7/8, pp. 496–509, Aug. 2010, doi: 10.1016/j.crhy.2010.05.001.

[2] M. Bolduc *et al.*, "Noise-equivalent power characterization of an uncooled microbolometer-based THz imaging camera," *Proc. SPIE*, vol. 8023, May 2011, Art. no. 80230C, doi: 10.1117/12.883507.

[3] F. Simoens and J. Meilhan, "Terahertz real-time imaging uncooled array based on antenna- and cavity-coupled bolometers," *Philosophical Trans. Ser. A Math. Physical Eng. Sci.*, vol. 372, no. 2012, Feb. 2014, Art. no. 20130111, doi: 10.1098/rsta.2013.0111.

[4] D.-T. Nguyen, F. Simoens, J.-L. Ouvrier-Buffet, J. Meilhan, and J.-L. Coutaz, "Broadband THz uncooled antenna-coupled microbolometer array—electromagnetic design, simulations and measurements," *IEEE Trans. Terahertz Sci. Technol.*, vol. 2, no. 3, pp. 299–305, May 2012, doi: 10.1109/TTHZ.2012.2188395.

[5] V. Mitin *et al.*, "Hot-electron micro & nanobolometers based on low-mobility 2DEG for high resolution THz spectroscopy," *J. Phys. Conf. Ser.*, vol. 486, Mar. 2014, Art. no. 012028, doi: 10.1088/1742-6596/486/1/012028.

[6] A. Semenov *et al.*, "Application of zero-bias quasi-optical Schottky-diode detectors for monitoring short-pulse and weak terahertz radiation," *IEEE Electron Device Lett.*, vol. 31, no. 7, pp. 674–676, Jul. 2010, doi: 10.1109/LED.2010.2048192.

[7] L. Liu, J. L. Hesler, H. Xu, A. W. Lichtenberger, and R. M. Weikle, "A broadband quasi-optical terahertz detector utilizing a zero bias Schottky diode," *IEEE Microw. Compon. Lett.*, vol. 20, no. 9, pp. 504–506, Sep. 2010, doi: 10.1109/LMWC.2010.2055553.

[8] O. Cojocari *et al.*, "Quasi optical Schottky diode detectors for fast ultra-wideband detection," in *Proc. IEEE Int. Conf. Microw. Millimeter Wave Technol.*, Jun. 2016, pp. 52–53, doi: 10.1109/ICMMT.2016.7761674.

[9] N. Su, R. Rajavel, P. Deelman, J. N. Schulman, and P. Fay, "Sb-heterostructure millimeter-wave detectors with reduced capacitance and noise equivalent power," *IEEE Electron Device Lett.*, vol. 29, no. 6, pp. 536–539, Jun. 2008, doi: 10.1109/LED.2008.922986.

[10] G. C. Trichopoulos, H. L. Mosbacker, D. Burdette, and K. Sertel, "A broadband focal plane array camera for real-time THz imaging applications," *IEEE Trans. Antennas Propag.*, vol. 61, no. 4, pp. 1733–1740, Apr. 2013, doi: 10.1109/TAP.2013.2242829.

[11] L. Liu, S. M. Rahman, Z. Jiang, W. Li, and P. Fay, "Advanced terahertz sensing and imaging systems based on integrated III-V interband tunneling devices," *Proc. IEEE*, vol. 105, no. 6, pp. 1020–1034, Jun. 2017, doi: 10.1109/JPROC.2016.2636245.

[12] T. Miyamoto, A. Yamaguchi, and T. Mukai, "Terahertz imaging system with resonant tunneling diodes," *Japanese J. Appl. Phys.*, vol. 55, no. 3, Mar. 2016, Art. no. 032201, doi: 10.7567/JJAP.55.032201.

[13] S. Diebold *et al.*, "Modeling and simulation of terahertz resonant tunneling diode-based circuits," *IEEE Trans. Terahertz Sci. Technol.*, vol. 6, no. 5, pp. 716–723, Sep. 2016, doi: 10.1109/TTHZ.2016.2592180.

[14] J. Torres *et al.*, "Nonlinear nanochannels for room temperature terahertz heterodyne detection," *Semicond. Sci. Technol.*, vol. 28, no. 12, Dec. 2013, Art. no. 125024, doi: 10.1088/0268-1242/28/12/125024.

[15] L. Minkevičius *et al.*, "Terahertz heterodyne imaging with InGaAs-based bow-tie diodes," *Appl. Phys. Lett.*, vol. 99, 2011, Art. no. 131101, doi: 10.1063/1.3641907.

[16] W. Knap *et al.*, "Field effect transistors for terahertz detection: Physics and first imaging applications," *J. Infrared Millimeter Terahertz Waves*, vol. 30, no. 12, pp. 1319–1337, 2009, doi: 10.1007/s10762-009-9564-9.

[17] F. Friederich *et al.*, "THz active imaging systems with real-time capabilities," *IEEE Trans. Terahertz Sci. Technol.*, vol. 1, no. 1, pp. 183–200, Sep. 2011, doi: 10.1109/TTHZ.2011.2159559.

[18] A. Rogalski and F. Sizov, "Terahertz detectors and focal plane arrays," *Opto-Electron. Rev.*, vol. 19, no. 3, Jan. 2011, doi: 10.2478/s11772-011-0033-3.

[19] M. Sakhno, A. Golenkov, and F. Sizov, "Uncooled detector challenges: Millimeter-wave and terahertz long channel field effect transistor and Schottky barrier diode detectors," *J. Appl. Phys.*, vol. 114, no. 16, Oct. 2013, Art. no. 164509, doi: 10.1063/1.4826364.

[20] A. Lisauskas *et al.*, "Exploration of terahertz imaging with silicon MOS-FETs," *J. Infrared Millimeter Terahertz Waves*, vol. 35, no. 1, pp. 63–80, Jan. 2014, doi: 10.1007/s10762-013-0047-7.

[21] J. Grzyb, B. Heinemann, and U. R. Pfeiffer, "A 0.55 THz near-field sensor with a μ m-range lateral resolution fully integrated in 130 nm SiGe BiCMOS," *IEEE J. Solid State Circuits*, vol. 51, no. 12, pp. 3063–3077, Dec. 2016, doi: 10.1109/JSSC.2012.2217851.

[22] P. Hillger, J. Grzyb, R. Jain, and U. R. Pfeiffer, "Terahertz imaging and sensing applications with silicon-based technologies," *IEEE Trans. Terahertz Sci. Technol.*, vol. 9, no. 1, pp. 1–19, Jan. 2019, doi: 10.1109/TTHZ.2018.2884852.

[23] E. Öjefors, U. Pfeiffer, A. Lisauskas, and H. G. Roskos, "A 0.65 THz focal-plane array in a quarter-micron CMOS process technology," *IEEE J. Solid State Circuits*, vol. 44, no. 7, pp. 1968–1976, Jun. 2009, doi: 10.1109/JSSC.2009.2021911.

[24] A. Lisauskas *et al.*, "Rational design of high-responsivity detectors of THz radiation based on distributed self-mixing in silicon CMOS transistors," *J. Appl. Phys.*, vol. 105, no. 11, 2009, Art. no. 114511, doi: 10.1063/1.3140611.

[25] M. Dyakonov and M. Shur, "Detection, mixing, and frequency multiplication of terahertz radiation by two-dimensional electronic fluid," *IEEE Trans. Electron Devices*, vol. 43, no. 3, pp. 380–387, Mar. 1996, doi: 10.1109/16.485650.

[26] T. Otsuji and M. Shur, "Terahertz plasmonics: Good results and great expectations," *IEEE Microw. Mag.*, vol. 15, no. 7, pp. 43–50, Nov. 2014, doi: 10.1109/MMM.2014.2355712.

[27] D. Glaab *et al.*, "Terahertz heterodyne detection with silicon field-effect transistors," *Appl. Phys. Lett.*, vol. 96, no. 4, Jan. 2010, Art. no. 042106, doi: 10.1063/1.3292016.

[28] S. Boppel *et al.*, "CMOS detector arrays in a virtual 10-kilopixel camera for coherent terahertz real-time imaging," *Opt. Lett.*, vol. 37, no. 4, pp. 536–538, 2012, doi: 10.1364/OL.37.000536.

[29] A. Lisauskas, S. Boppel, M. Mundt, V. Krozer, and G. Roskos, "Sub-harmonic mixing with field-effect transistors: Theory and experiment at 639 GHz high above f_T," *IEEE Sensors J.*, vol. 13, no. 1, pp. 124–132, Jan. 2013, doi: 10.1109/JSEN.2012.2223668.

[30] C. Jiang *et al.*, "A fully integrated 320 GHz coherent imaging transceiver in 130 nm SiGe BiCMOS," *IEEE J. Solid-State Circuits*, vol. 51, no. 11, pp. 2596–2609, Nov. 2016, doi: 10.1109/JSSC.2016.2599533.

[31] A. Lisauskas *et al.*, "Field-effect transistors as electrically controllable nonlinear rectifiers for the characterization of terahertz pulses," *APL Photonics*, vol. 3, no. 5, 2018, Art. no. 051705, doi: 10.1063/1.5011392.

[32] F. Schuster *et al.*, "Broadband terahertz imaging with highly sensitive silicon CMOS detectors," *Opt. Express*, vol. 19, no. 8, pp. 7827–7832, 2011, doi: 10.1364/OE.19.007827.

[33] R. Al Hadi *et al.*, "A 1 k-pixel video camera for 0.7-1.1 terahertz imaging applications in 65-nm CMOS," *IEEE J. Solid-State Circuits*, vol. 47, no. 12, pp. 2999–3012, Dec. 2012, doi: 10.1109/JSSC.2012.2217851.

[34] S. Boppel *et al.*, "CMOS integrated antenna-coupled field-effect transistors for the detection of radiation from 0.2 to 4.3 THz," *IEEE Trans. Microw. Theory Techn.*, vol. 60, no. 12, pp. 3834–3843, Dec. 2012, doi: 10.1109/TMTT.2012.2221732.

[35] M. Bauer *et al.*, "High-sensitivity wideband THz detectors based on GaN HEMTs with integrated bow-tie antennas," in *Proc. 10th Eur. Microw. Integr. Circuits Conf.*, Dec. 2015, pp. 1–4, doi: 10.1109/EuMIC.2015.7345053.

[36] K. Ikamas *et al.*, "Broadband terahertz power detectors based on 90-nm silicon CMOS transistors with flat responsivity up to 2.2 THz," *IEEE Electron Device Lett.*, vol. 39, no. 9, pp. 1413–1416, Sep. 2018, doi: 10.1109/LED.2018.2859300.

[37] M. Bauer *et al.*, "Antenna-coupled field-effect transistors for multi-spectral terahertz imaging up to 4.25 THz," *Opt. Express*, vol. 22, no. 16, Aug. 2014, Art. no. 19235, doi: 10.1364/OE.22.019235.

[38] J. D. Sun *et al.*, "High-responsivity, low-noise, room-temperature, self-mixing terahertz detector realized using floating antennas on a GaN-based field-effect transistor," *Appl. Phys. Lett.*, vol. 100, no. 1, Jan. 2012, Art. no. 013506, doi: 10.1063/1.3673617.

[39] U. R. Pfeiffer, J. Grzyb, H. Sherry, A. Cathelin, and A. Kaiser, "Toward low-NEP room-temperature THz MOSFET direct detectors in CMOS technology," in *Proc. IEEE 38th Int. Conf. Infrared, Millimeter, Terahertz Waves*, 2013, pp. 1–2, doi: 10.1109/IRMMW-THz.2013.6665522.

[40] F. H. L. Koppens *et al.*, "Photodetectors based on graphene, other two-dimensional materials and hybrid systems," *Nat. Nanotechnol.*, vol. 9, no. 10, pp. 780–793, Oct. 2014, doi: 10.1038/nnano.2014.215.

[41] A. Zak *et al.*, "Antenna-integrated 0.6 THz FET direct detectors based on CVD graphene," *Nano Lett.*, vol. 14, no. 10, pp. 5834–5838, Oct. 2014, doi: 10.1021/nl5027309.

[42] J. Al-Eryani *et al.*, "Fully integrated single-chip 305–375-GHz transceiver with on-chip antennas in SiGe BiCMOS," *IEEE Trans. Terahertz Sci. Technol.*, vol. 8, no. 3, pp. 329–339, May 2018, doi: 10.1109/TTHZ.2018.2823202.

[43] S. J. Pearton *et al.*, "Review—Ionizing radiation damage effects on GaN devices," *ECS J. Solid State Sci. Technol.*, vol. 5, no. 2, pp. Q35–Q60, Nov. 2015, doi: 10.1149/2.0251602jss.

[44] A. V. Muravjov *et al.*, "Temperature dependence of plasmonic terahertz absorption in grating-gate gallium-nitride transistor structures," *Appl. Phys. Lett.*, vol. 96, 2010, Art. no. 042105, doi: 10.1063/1.3292019.

[45] M. Sakowicz *et al.*, "Terahertz responsivity of field effect transistors versus their static channel conductivity and loading effects," *J. Appl. Phys.*, vol. 110, 2011, Art. no. 054512, doi: 10.1063/1.3632058.

[46] O. A. Klimenko *et al.*, "Temperature enhancement of terahertz responsivity of plasma field effect transistors," *J. Appl. Phys.*, vol. 112, 2012, Art. no. 014506, doi: 10.1063/1.4733465.

[47] M. Bauer *et al.*, "Bow-tie-antenna-coupled terahertz detectors using AlGaN/GaN field-effect transistors with 0.25 micrometer gate length," in *Proc. 8th Eur. Microw. Integr. Circuits Conf.*, Dec. 2013, pp. 212–215.

[48] J. Sun *et al.*, "The effect of symmetry on resonant and nonresonant photoresponses in a field-effect terahertz detector," *Appl. Phys. Lett.*, vol. 106, no. 3, 2015, Art. no. 031119, doi: 10.1063/1.4906536.

[49] N. Dyakonova *et al.*, "Saturation of photoresponse to intense THz radiation in AlGaN/GaN HEMT detector," *J. Appl. Phys.*, vol. 89, 2016, Art. no. 164507, doi: 10.1063/1.4966575.

[50] H. Spisser *et al.*, "Room-temperature AlGaN/GaN terahertz plasmonic detectors with a zero-bias grating," *J. Infrared Millimeter Terahertz. Waves*, vol. 37, pp. 243–257, Nov. 2016, doi: 10.1007/s10762-015-0224-y.

[51] S. Boppel *et al.*, "0.25-μ m GaN TeraFETs optimized as THz power detectors and intensity-gradient sensors," *IEEE Trans. Terahertz Sci. Technol.*, vol. 6, no. 2, pp. 348–350, Mar. 2016, doi: 10.1109/TTHZ.2016.2520202.

[52] H. W. Hou *et al.*, "High temperature terahertz detectors realized by a GaN high electron mobility transistor," *Sci. Rep.*, vol. 7, 2017, Art. no. 46664, doi: 10.1038/srep46664.

[53] H. Qin *et al.*, "Detection of incoherent terahertz light using antenna-coupled high-electron-mobility field-effect transistors," *Appl. Phys. Lett.*, vol. 110, no. 17, Apr. 2017, Art. no. 171106, doi: 10.1063/1.4982604.

[54] H. Hou *et al.*, "A sub-terahertz broadband detector based on a GaN high-electron-mobility transistor with nanoantennas," *Appl. Phys. Express*, vol. 10, 2018, Art. no. 014101, doi: 10.7567/APEX.10.014101.

[55] D. Voß *et al.*, "Imaging and spectroscopic sensing with low-repetition-rate terahertz pulses and GaN TeraFET detectors," *J. Infrared Millimeter Terahertz Waves*, vol. 39, no. 3, pp. 262–272, 2018, doi: 10.1007/s10762-017-0447-1.

[56] M. A. Andersson and J. Stake, "An accurate empirical model based on Volterra series for FET power detectors," *IEEE Trans. Microw. Theory Techn.*, vol. 64, no. 5, pp. 1431–1441, May 2016, doi: 10.1109/TMTT.2016.2532326.

[57] L. Vicarelli *et al.*, "Graphene field-effect transistors as room-temperature terahertz detectors," *Nature Mater.*, vol. 11, no. 10, pp. 865–871, 2012, doi: 10.1038/NMAT3417.

[58] L. Viti *et al.*, "Efficient Terahertz detection in black-phosphorus nanotransistors with selective and controllable plasma-wave, bolometric and thermoelectric response," *Sci. Rep.*, vol. 6, Feb. 2016, Art. no. 20474, doi: 10.1038/srep20474.

[59] M. Bauer *et al.*, "Optimization of the design of terahertz detectors based on Si CMOS and AlGaN/GaN field-effect transistors," *Int. J. High Speed Electron.*, vol. 25, no. 03n04, Sep. 2016, Art. no. 1640013, doi: 10.1142/S0129156416400139.

[60] J. Vyšniauskas *et al.*, "Hydrodynamic modelling of terahertz rectification in AlGaN/GaN high electron mobility transistors," *J. Phys. Conf. Ser.*, vol. 906, Oct. 2017, Art. no. 012023, doi: 10.1088/1742-6596/906/1/012023.

[61] S. Regensburger *et al.*, "Broadband THz detection from 01 to 22 THz with large area field-effect transistors," *Opt. Express*, vol. 23, no. 16, Aug. 2015, Art. no. 20732, doi: 10.1364/OE.23.020732.

[62] A. El Fatimy *et al.*, "Resonant and voltage-tunable terahertz detection in InGaAs/InP nanometer transistors," *Appl. Phys. Lett.*, vol. 89, 2006, Art. no. 131926, doi: 10.1063/1.2358816.

[63] S. Kang, P. J. Burke, L. N. Pfeiffer, and K. W. West, "Resonant frequency response of plasma wave detectors," *Appl. Phys. Lett.*, vol. 89, Nov. 2006, Art. no. 213512, doi: 10.1063/1.2393023.

[64] A. Shchepetov *et al.*, "Oblique modes effect on terahertz plasma wave resonant detection in InGaAs/InAlAs multichannel transistors," *Appl. Phys. Lett.*, vol. 92, Jun. 2008, Art. no. 242105, doi: 10.1063/1.2945286.

[65] G. C. Dyer *et al.*, "Enhanced performance of resonant sub-terahertz detection in a plasmonic cavity," *Appl. Phys. Lett.*, vol. 100, Feb. 2012, Art. no. 083506, doi: 10.1063/1.3687698.

[66] T. Otsuji *et al.*, "Emission and detection of terahertz radiation using two-dimensional plasmons in semiconductor nanoheterostructures for nondestructive evaluations," *Opt. Eng.*, vol. 53, Mar. 2014, Art. no. 031206, doi: 10.1117/1.OE.53.3.031206.

[67] D. A. Bandurin *et al.*, "Resonant terahertz detection using graphene plasmons," *Nature Commun.*, vol. 9, 2018, Art. no. 5392, doi: 10.1038/s41467-018-07848-w.

[68] I. Khmyrova and Y. Seijyou, "Analysis of plasma oscillations in high-electron mobility transistorlike structures: Distributed circuit approach," *Appl. Phys. Lett.*, vol. 91, 2007, Art. no. 143515, doi: 10.1063/1.2794772.

[69] S. Preu *et al.*, "An improved model for non-resonant terahertz detection in field-effect transistors," *J. Appl. Phys.*, vol. 111, no. 2, Jan. 2012, Art. no. 024502, doi: 10.1063/1.3676211.

[70] A. Lisauskas *et al.*, "Terahertz responsivity and low-frequency noise in biased silicon field-effect transistors," *Appl. Phys. Lett.*, vol. 102, no. 15, 2013, Art. no. 153505, doi: 10.1063/1.4802208.

[71] D. Čibiraitė *et al.*, "Thermal noise-limited sensitivity of FET-based terahertz detectors," in *Proc. Int. Conf. Noise Fluctuations*, Jun. 2017, pp. 1–4, doi: 10.1109/ICNF.2017.7986008.

[72] *CST Studio Suite*. (2018). CST—Computer Simulation Technology GmbH.

[73] D. F. Filipovic, S. S. Gearhart, and G. M. Rebeiz, "Double-slot antennas on extended hemispherical and elliptical silicon dielectric lenses," *IEEE Trans. Microw. Theory Techn.*, vol. 41, no. 10, pp. 1738–1749, Oct. 1993, doi: 10.1109/22.247919.

[74] S. Khandelwal, N. Goyal, and T. A. Fjeldly, "A physics-based analytical model for 2DEG charge density in AlGaN/GaN HEMT devices," *IEEE Trans. Electron Devices*, vol. 58, no. 10, pp. 3622–3625, Oct. 2011, doi: 10.1109/TED.2011.2161314.

[75] M. Shur, T. A. Fjeldly, T. Ytterdal, and K. Lee, "Unified MOSFET model," *Solid State Electron.*, vol. 35, no. 12, pp. 1795–1802, Dec. 1992, doi: 10.1016/0038-1101(92)90263-C.

[76] T. Grasser, T.-W. Tang, H. Kosina, and S. Selberherr, "A review of hydrodynamic and energy-transport models for semiconductor device simulation," *Proc. IEEE*, vol. 91, no. 2, pp. 251–274, Feb. 2003, doi: 10.1109/JPROC.2002.808150.

[77] Thomas Keating Ltd, "Absolute terahertz power/energy meter," 2017. [Online]. Available: www.terahertz.co.uk/tk-instruments/products/absolute-thz-power-energy-meters

[78] TOPTICA Photonics AG, "Terascan 1550," 2017. [Online]. Available: www.toptica.com/products/terahertz-systems/frequency-domain/terascan

[79] A. J. Deninger, A. Roggenbuck, S. Schindler, and S. Preu, "2.75 THz tuning with a triple-DFB laser system at 1550 nm and InGaAs photomixers," *J. Infrared Millimeter Terahertz Waves*, vol. 36, no. 3, pp. 269–277, Mar. 2015, doi: 10.1007/s10762-014-0125-5.

[80] J. Van Rudd and D. M. Mittleman, "Influence of substrate-lens design in terahertz time-domain spectroscopy," *J. Opt. Soc. Amer. B*, vol. 19, no. 2, pp. 319–329, Feb. 2002, doi: 10.1364/JOSAB.19.000319.

[81] A. Lisauskas *et al.*, "Terahertz imaging with Si MOSFET focal-plane arrays," *Proc. SPIE*, vol. 72150, 2009, Art. no. 72150J, doi: 10.1117/12.809552.

[82] TYDEX, "Golay detectors," 2018. [Online]. Available: www.tydexoptics.com/products/thz_devices/golay_cell

[83] LASER COMPONENTS GmbH, "LiTaO3 single channel detector," 2018. [Online]. Available: www.lasercomponents.com/de-en/ir-components/pyroelectric-detectors

[84] J. K. Choi *et al.*, "THz hot-electron micro-bolometer based on low-mobility 2-DEG in GaN heterostructure," *IEEE Sensors J.*, vol. 13, no. 1, pp. 80–88, Jan. 2013, doi: 10.1109/JSEN.2012.2224334.

[85] M. Yahyapour *et al.*, "A flexible phase-insensitive system for broadband CW-terahertz spectroscopy and imaging," *IEEE Trans. Terahertz Sci. Technol.*, vol. 6, no. 5, pp. 670–673, Sep. 2016, doi: 10.1109/TTHZ.2016.2589540.

[86] ACST GmbH, "Quasi-optical THz detectors," 2018. [Online]. Available: www.acst.de/products/quasi-optical-detectors

[87] Virginia Diodes, Inc., "Quasi-optical, zero-bias Schottky diode detector," 2019. [Online]. Available: www.vadiodes.com/en/products/detectors

[88] I. Kašalynas *et al.*, "Design and performance of a room-temperature terahertz detection array for real-time imaging," *IEEE J. Sel. Top. Quantum Electron.*, vol. 14, no. 2, pp. 363–369, Mar./Apr. 2008, doi: 10.1109/JSTQE.2007.912629.

[89] J. Zdanevicius *et al.*, "Field-effect transistor-based detectors for power monitoring of THz quantum cascade lasers," *IEEE Trans. Terahertz Sci. Technol.*, vol. 8, no. 6, pp. 613–621, Nov. 2018, doi: 10.1109/TTHZ.2018.2871360.

[90] H. Sherry *et al.*, "Lens-integrated THz imaging arrays in 65nm CMOS technologies," in *Proc. IEEE Radio Freq. Integr. Circuits Symp.*, 2011, pp. 1–4.

[91] K. Sengupta, D. Seo, L. Yang, and A. Hajimiri, "Silicon integrated 280 GHz imaging chipset with 4×4 SiGe receiver array and CMOS source," *IEEE Trans. Terahertz Sci. Technol.*, vol. 5, no. 3, pp. 427–437, May 2015, doi: 10.1109/TTHZ.2015.2414826.

[92] U. R. Pfeiffer, E. Öjefors, A. Lisauskas, and H. G. Roskos, "Opportunities for silicon at mmWave and terahertz frequencies," in *Proc. IEEE Bipolar/BiCMOS Circuits Technol. Meeting*, Oct. 2008, pp. 149–156, doi: 10.1109/BIPOL.2008.4662734.

[93] S. M. Rahman, Z. Jiang, I. B. Shams, P. Fay, and L. Liu, "A G-Band monolithically integrated quasi-optical zero-bias detector based on heterostructure backward diodes using submicrometer airbridges," *IEEE Trans. Microw. Theory Tech.*, vol. 66, no. 4, pp. 2010–2017, Apr. 2018, doi: 10.1109/TMTT.2017.2779133.

[94] Z. Ahmad, A. Lisauskas, H. G. Roskos, and K. K. O , "9.74-THz electronic Far-Infrared detection using Schottky barrier diodes in CMOS," in *2014 IEEE Int. Electron Devices Meeting*, Dec. 2014, pp. 4.4.1–4.4.4, doi: 10.1109/IEDM.2014.7046982.

[95] V. G. Bozhkov, "Semiconductor detectors, mixers, and frequency multipliers for the terahertz band," *Radiophys. Quantum Electron.*, vol. 46, no. 8/9, pp. 631–656, Aug. 2003, doi: 10.1023/B:RAQE.0000024993.40125.2b.

[96] A. K. Huhn *et al.*, "Uncooled antenna-coupled terahertz detectors with 22 μ s response time based on BiSb/Sb thermocouples," *Appl. Phys. Lett.*, vol. 102, no. 12, Mar. 2013, Art. no. 121102, doi: 10.1063/1.4798369.

[97] W. H. Steel, "The design of reflecting microscope objectives," *Australian J. Sci. Res., Ser. A. Physical Sci.*, vol. 4, no. 1, pp. 1–11, Mar. 1951.

[98] M. Bauer *et al.*, "The potential for sensitivity enhancement by the thermoelectric effect in carbon-nanotube and graphene tera-FETs," *J. Phys. Conf. Ser.*, vol. 647, Oct. 2015, Art. no. 012004, doi: 10.1088/1742-6596/647/1/012004.

Maris Bauer was born in Frankfurt am Main, Germany, in 1985. He received the doctoral degree in physics from Goethe University Frankfurt, Frankfurt, Germany, in 2018, working on the modeling of charge carrier transport and photo-thermoelectric effects in TeraFETs, and the implementation and characterization of devices in different materials including novel carbon-based materials and III-V semiconductors.

From 2008 to 2014, he was a Research Assistant with SynView GmbH. In 2017, he joined the Center for Materials Characterization and Testing, Fraunhofer ITWM, Germany, working on terahertz applications and system design.

Dovilė Čibiraitė received the B.S. degree in modern technologies physics and management and the M.S. degree in telecommunications physics and electronics from Vilnius University, Vilnius, Lithuania, in 2014 and 2016, respectively.

Her research on Terahertz rectification in monolayer graphene field-effect transistors led her to continue her research in THz radiation field. In 2016, she was awarded with a Marie Sklodowska-Curie Actions Grant to conduct a Ph.D. research on the topic "THz camera based on GaN plasmonic FET devices" at the Department of Physics, Goethe University Frankfurt, Frankfurt, Germany. Her research interest includes plasmonic THz detectors, such as graphene FETs and GaN HEMTs.

Adam Rämer received the Dipl.-Ing. in electrical engineering from the Technical University of Berlin, Berlin, Germany, in 2012.

Since 2012, he has been a Research Associate with the Joint Lab THz Components and Systems, Ferdinand-Braun-Institut (FBH), Berlin, Germany, where he is involved in the development and design of GaN HEMT-based broadband THz detectors. His research interests include power amplifiers, broadband antennas, GaN HEMTs for special applications, MMIC design, and THz measurement.

Sandra Pralgauskaitė was born in 1975, in Kaunas, Lithuania. She received the bachelor's degree in radiophysics and the master's degree in telecommunication physics from Vilnius University, Vilnius, Lithuania, in 1997 and 1999, respectively, and the doctorate degree in physical science with the doctoral dissertation topic "Optical and electrical low-frequency noise characteristics of multimode and singlemode InGaAsP/InP multiple-quantum well laser diodes," from the Semiconductor Physics Institute, Vilnius, Lithuania, in 2003.

Since 2003, she has been a Senior Researcher with the Department of Radiophysics, Vilnius University. Her research interests include optoelectronic devices, noise characterization, and quality and reliability of electronic and optoelectronic devices.

Serguei A. Chevtchenko received the Diploma degree in solid state physics from Moscow Engineering Physics Institute, Moscow, Russia, in 1998, and the Ph.D. degree in engineering from Virginia Commonwealth University, Richmond, VA, USA, in 2007, where he conducted experimental studies of structural, optical, and electronic properties of wide bandgap semiconductors (GaN and ZnO).

In 2008, he joined Ferdinand-Braun-Institut (FBH), Berlin, Germany. His responsibilities at FBH include the development and technical coordination of processes for the fabrication of GaN-based MMICs and high power microwave transistors as well as the analysis of dc and microwave characterization results. He is involved in the fabrication process and layout optimization of the broadband GaN-based THz detectors and arrays.

Kęstutis Ikamas received the Diploma in physics in 1995 and the doctorate degree working on the modeling of broadband THz detectors with field-effect transistors and the application of these devices for systems with pulsed and dc sources, in 2018, from Vilnius University, Vilnius, Lithuania.

He is currently with the Noise and Terahertz Electronics Group, Vilnius University, where he is involved in the area of CMOS transistor-based terahertz detectors' and sources' design, modeling, and application.

Konstantin Y. Osipov received the master's degree in electrical engineering from the Tomsk State University of Control Systems and Radio Electronics, Russia, in 2008, where he worked on the technology of GaAs based commutation MMICs.

In the research and production company "Micran", Russia, he developed various process modules for GaN HEMT fabrication. In 2012, he joined Ferdinand-Braun-Institut (FBH) in Berlin as a DAAD student, where he has been responsible for deep submicron GaN HEMT's gate fabrication process development. Since 2013, he has been continuing this work as a PhD Student working on high frequency, highly reliable GaN MMICs for space applications. Since 2017, he has been employed at Ampleon B.V. Netherlands as a Senior GaN Technology Engineer, responsible for the development and integration of multiapplication GaN HEMT technology.

Alvydas Lisauskas (M'18) received the Diploma in physics from Vilnius University, Vilnius, Lithuania, in 1995, and the Ph.D. degree from the Royal Institute of Technology, Stockholm, Sweden, in 2001.

In 2002, he was a Postdoctor with the Ultrafast Spectroscopy and Terahertz Physics Group, Goethe University Frankfurt, Frankfurt, Germany, working on novel semiconductor devices for THz applications. Since 2014, he has been a Professor with Vilnius University and a Leading Researcher with the Center for Physical Science and Technology, Vilnius, Lithuania. Since February 2019, he has been a Group Leader on Terahertz Electronics with the Center for Terahertz Research and Applications, Institute of High Pressure Physics PAS, Warsaw, Poland. His research interests include terahertz electronics, design and modeling of semiconductor devices, and terahertz imaging techniques.

Wolfgang Heinrich (M'84–SM'95–F'09) received the Diploma, Ph.D., and Habilitation degrees in electrical engineering from the Technical University of Darmstadt, Darmstadt, Germany, in 1983, 1987, and 1992, respectively.

Since 1993, he has been with Ferdinand-Braun-Institut (FBH), Berlin, Germany, where he is the Head of the Department of Microwave and the Deputy Director of the Institute. Since 2008, he has also been a Professor with the Technical University of Berlin, Berlin, Germany. He has authored or coauthored more than 350 publications and conference contributions. His research interests include MMIC design with emphasis on GaN power amplifiers, mm-wave integrated circuits, and electromagnetic simulation.

Dr. Heinrich has been serving the microwave community in various functions, e.g., as a Distinguished Microwave Lecturer for the term 2003–2005, as the General Chair of the European Microwave Week in Munich, 2007, and as an Associate Editor for the IEEE TRANSACTIONS ON MICROWAVE THEORY AND TECHNIQUES from 2008 to 2010. From 2010 through 2018, he was the President of the European Microwave Association (EuMA).

Viktor Krozer (M'91–SM'03) received the Dipl.-Ing. and Dr.-Ing. degrees in electrical engineering from Technical University Darmstadt, Darmstadt, Germany, in 1984 and 1991, respectively.

In 1991, he was a Senior Scientist with Technical University Darmstadt working on high-temperature microwave devices and circuits and submillimeter-wave electronics. From 1996 to 2002, he was a Professor with the Technical University of Chemnitz, Germany. From 2002 to 2009, he was a Professor in electromagnetic systems, with DTU Elektro, Technical University of Denmark, and was the Head of the Microwave Technology Group. Since 2009, he has been an endowed Oerlikon-Leibniz-Goethe Professor in terahertz photonics with Goethe University Frankfurt, Frankfurt, Germany, and heads the Goethe-Leibniz-Terahertz-Center. He is also with Ferdinand-Braun-Institut (FBH), Berlin, Germany, leading the THz Components and Systems Group. His research interests include terahertz electronics, MMIC, nonlinear circuit analysis and design, device modeling, and remote sensing instrumentation.

Hartmut G. Roskos received the Vordiplom degree in physics from the Technical University of Karlsruhe, Karlsruhe, Germany, in 1981, the Diploma degree in physics and the Ph.D. degree from the Technical University of Munich, Munich, Germany, in 1985 and 1989, respectively, and the Habilitation degree for his work on coherent phenomena in solid-state physics from RWTH Aachen, Aachen, Germany, in 1996.

He was a Postdoctor with the AT&T Bell Laboratories, Holmdel, NJ, USA, where THz phenomena became the focus of his research. From 1991 to 1996, he was with the Institute of Semiconductor Electronics, RWTH Aachen. Since 1997, he has been a Full Professor with Goethe University Frankfurt, Frankfurt, Germany. He spent sabbaticals at UCSB in 2005, Osaka University in 2009/2010, and the University of Rochester in 2014. His research interests include ultrafast optical and THz spectroscopy, s-SNOM nanoscopy, THz device physics, and applications of THz radiation.

Dr. Roskos was the recipient of a five-year endowed professorship, in 2009, by OC Oerlikon AG jointly with Ferdinand-Braun-Institute (FBH), Berlin, Germany, which led to the establishment of a JointLab for THz Photonics of FBH and Goethe University Frankfurt, now led by Prof. Dr. Viktor Krozer. Since 2015, he has been a Topical Editor for *Optics Letters*.